

GT2009-60185

HEAT TRANSFER FOR A TURBINE BLADE WITH NON-AXISYMMETRIC ENDWALL CONTOURING

Stephen P. Lynch
Narayan Sundaram
Karen A. Thole

Mechanical and Nuclear Engineering Department
The Pennsylvania State University
University Park, PA 16802, USA

Atul Kohli
Christopher Lehane

Pratt & Whitney
400 Main Street
East Hartford, CT 06108, USA

ABSTRACT

Complex vortical secondary flows that are present near the endwall of an axial gas turbine blade are responsible for high heat transfer rates and high aerodynamic losses. The application of non-axisymmetric, three-dimensional contouring to the endwall surface has been shown to reduce the strength of the vortical flows and decrease total pressure losses when compared to a flat endwall. The reduction of secondary flow strength with non-axisymmetric contouring might also be expected to reduce endwall heat transfer.

In this study, measurements of endwall heat transfer were taken for a low-pressure turbine blade geometry with both flat and three-dimensional contoured endwalls. Endwall oil flow visualization indicated a reduction in the passage vortex strength for the contoured endwall geometry. Heat transfer levels were reduced by 20 percent in regions of high heat transfer with the contoured endwall, as compared to the flat endwall. The heat transfer benefit of the endwall contour was not affected by changes in the cascade Reynolds number.

INTRODUCTION

A fundamental issue in the design of gas turbine engines is the detrimental effects of vortical flows that are present near the junction of the airfoil and its endwall. These flows, generally termed secondary flows, increase aerodynamic losses through the turbine, leading to lower overall engine efficiency. Furthermore, the vortical flows result in high heat transfer rates due to mean flow distortion and high turbulence levels. For highly loaded parts such as the low-pressure turbine blade in this study, part durability can be significantly impacted by high heat transfer. It is obvious that reducing or eliminating the effects of the secondary flows would result in appreciable benefits in an engine, and thus much research has been conducted to understand these flows and control them.

Past research has shown that three-dimensional modifications to the endwall surface, generally referred to as non-axisymmetric contouring, are an effective method of reducing or eliminating secondary flows. Peaks and valleys in the endwall locally decrease or increase the static pressure, respectively, which can reduce the pressure gradient between adjacent airfoils that strengthens secondary flows. Weaker secondary flows result in lower aerodynamic losses, as has been documented by many researchers. However, few studies have considered the effect of non-axisymmetric contouring on endwall heat transfer, and thus the overall benefit of contouring in an engine is not completely understood as of yet.

This paper discusses the effect of non-axisymmetric contouring on the endwall heat transfer for a low-pressure turbine blade. The effect of varying the cascade Reynolds number for both the flat and contoured endwalls is also considered.

NOMENCLATURE

b	turbulence grid bar width
BL	boundary layer
C	true chord of blade
C_{ax}	axial chord of blade
C_p	specific heat at constant pressure, or static pressure coefficient, $C_p = (P_s - P_{s,in}) / 0.5\rho U_{\infty,in}^2$
h	heat transfer coefficient, $h = q''_w / (T_w - T_{\infty,in})$
H	boundary layer shape factor
k	thermal conductivity
Nu	Nusselt number, $Nu = hC_{ax} / k_{air}$
P	blade pitch
P_s	static pressure
q''_w	wall heat flux

Re_{exit}	cascade exit Reynolds number, $Re_{exit} = C_{ax} U_{\infty,exit} / \nu$
Re_s	boundary layer Reynolds number, $Re_s = sU_{\infty} / \nu$
s	distance from start of velocity boundary layer, or surface distance along airfoil
S	blade span
St	Stanton number, $St = h / \rho C_p U_{\infty}$
T	temperature
T_{reflc}	average temperature associated with radiation reflected off the endwall from the surroundings
x	streamwise distance downstream of the turbulence grid
X, Y, Z	global coordinates, where X is blade axial direction
U	streamwise velocity

Greek

δ	boundary layer thickness
δ^*	displacement thickness
ε	emissivity
θ	momentum thickness
ν	kinematic viscosity
ρ	density

Subscripts

exit	exit conditions
in	inlet conditions
w	wall conditions
∞	local freestream conditions

Superscripts

+	boundary layer inner coordinates
'	rms of fluctuating parameter

RELEVANT PAST STUDIES

Given our current understanding of secondary flow (e.g., the endwall flow models of Langston et al. [1], Sharma and Butler [2], and Goldstein and Spores [3]), attempts to eliminate such flow have focused on influencing the horseshoe vortex and/or the passage vortex development. Manipulation of the endwall-airfoil geometry has shown the most promise in this area, and can be loosely categorized into modifications of the airfoil leading edge (not addressed here), and modifications to the entire passage endwall.

Endwall-airfoil geometry can be altered to reduce secondary flows through the use of a contour. This category might be further subdivided into axisymmetric contouring (contour shape is only a function of axial coordinate), and non-axisymmetric contouring (contour shape is three-dimensional). Although axisymmetric contouring has been successful at reducing exit losses and surface heat transfer (e.g., see Boletis [4], Morris and Hoare [5], and Lin and Shih [6]), it has generally only been applied to stator vanes and is not considered further here.

Non-axisymmetric contouring has also demonstrated significant improvements in turbine performance, and is the

focus of this study. A computational optimization study by Harvey et al. [7] produced a three-dimensional blade endwall contour intended to minimize exit flow angle deviations and pitchwise static pressure gradients. The optimum design had convex endwall curvature near the pressure side and concave curvature at the suction side in the front of the passage to reduce cross-passage pressure gradients, while convex curvature near the trailing edge suction side reduced exit flow angle deviation. Unfortunately, it was also noted that a strong corner vortex developed near the suction side trailing edge. Experimental validation by Hartland et al. [8] confirmed the general conclusions of Harvey et al. [7], and found that net secondary losses decreased by 30% for the contoured wall relative to a flat wall. Brennan et al. [9] and Rose et al. [10] used the design method of Harvey et al. [7] on a Trent 500 high-pressure turbine stage and demonstrated 0.59% stage efficiency improvement. Recently, Germain et al. [11] and Scheupbach et al. [12] examined the effect of non-axisymmetric contouring of the stator and rotor endwalls in a 1-1/2 stage turbine. Overall stage efficiency was improved by 1.0%±0.4%, which was largely attributed to reductions in the stator time-averaged and unsteady losses.

Saha and Acharya [13] presented the first known study to consider the effect of non-axisymmetric contouring on the endwall heat transfer for a high-pressure turbine blade. They computationally evaluated nine endwall shapes and found that the best design reduced overall heat transfer by 8%, with significant reductions of over 300% near the suction side leading edge and approximately 20% in the throat compared to a flat endwall. Gustafson et al. [14] reported aerodynamic measurements for the same airfoil and contoured endwall. They found a stronger suction side horseshoe vortex and a weaker passage vortex, which resulted in a measured overall loss reduction of 50% relative to a flat endwall. However, their smoke flow visualization (at a lower cascade Reynolds number) indicated that the saddle point moved farther from the blade leading edge for the contour, in contradiction to Saha and Acharya's [13] conclusions. Furthermore, Saha and Acharya's results did not indicate a stronger suction side horseshoe vortex.

Praisner et al. [15] and Knezevici et al. [16] examined non-axisymmetric contouring for the same low-pressure turbine blade as in this study. Praisner et al. [15] used computational optimization based on secondary loss reduction to design non-axisymmetric endwall contours for the Pack-B airfoil, as well as for a related family of high-lift airfoils (Pack-D fore- and aft-loaded). The Pack-B endwall contour reduced losses (4% predicted, 10% measured) and turbulent kinetic energy levels associated with the secondary flow, when compared to the flat endwall. Knezevici et al. [16] presented oil flow visualization and seven-hole probe measurements that showed a reduction in passage vortex strength with the contour, although the corner vortex and near-wall passage crossflow were intensified near the trailing edge where the contour merged back to the flat endwall level.

The study reported in this paper expands on the work of Praisner et al. [15] and Knezevici et al. [16] by considering the effect of non-axisymmetric contouring on endwall heat transfer for the same low-pressure turbine blade. Although the heat loads for low-pressure turbine blades are not as critical as for high-pressure turbine blades, part durability is still a design consideration, especially given the trend of highly loading the low-pressure turbine to lower airfoil count (Praisner et al. [17]). Also considered in this study is the effect of cascade Reynolds number on the endwall heat transfer for the flat and contoured geometries.

EXPERIMENTAL METHODOLOGY

Endwall heat transfer measurements, with and without a three-dimensional contoured endwall, were obtained in a newly constructed test section containing seven scaled-up turbine blades based on the low-pressure turbine Pack-B airfoil geometry. Flow through the test section was supplied by a large-scale low-speed wind tunnel, depicted in Figure 1a. For this tunnel, the large scale allows engine Reynolds numbers to be matched, and provides for high resolution measurements. Flow through the tunnel's closed loop was powered by an axial fan, was cooled by a heat exchanger, and then passed through a series of flow conditioning screens before entering the convergence section.

The convergence, shown in Figure 1b, was designed to reduce the flow area from 1.11 m^2 to 0.62 m^2 by symmetric quarter-round sections on the top and bottom walls, and was located nearly 11 axial chords upstream of the center blade. An analysis of the variation in boundary layer thickness in the pitch direction across the blade cascade, which was angled to match the blade inlet flow angle, indicated that δ/S would vary $\pm 11\%$ relative to the boundary layer approaching the center blade. Details of the measured boundary layer are presented later.

Immediately downstream of the convergence, a passive bar grid was mounted in the flowpath. The grid consisted of 2.54 cm square bars, separated by 10.2 cm from center to center. The grid bar width, spacing, and location upstream of the

cascade were designed using the results of Baines and Peterson [18] to achieve a freestream turbulence level of approximately 4% at the inlet plane of the blade cascade. A prediction of the turbulence intensity across the blade inlet plane in the pitch direction indicated that the turbulence intensity would range from 3.9% at the blade farthest downstream of the grid, to 4.8% at the blade closest to the grid. Measurements of the turbulence decay downstream of the grid are presented later.

As mentioned previously, a new test section was constructed to house seven blades, based on the Pack-B airfoil geometry and scaled to 8.6 times engine scale. The blade geometry and nominal flow conditions are given in Table 1. The Pack-B blade was designed for studies of low-pressure turbine aerodynamics in low-speed cascades. It is a highly-loaded blade (Zweifel coefficient of 1.13), and its aerodynamic characteristics have been reported extensively in the literature ([15]-[17], [19]-[23]). Figure 2a shows a top view of the cascade, which had adjustable bleed flaps on the sides of the lower blade (blade 1) and upper blade (blade 7) to control the uniformity of the velocity entering the cascade. Tailboards attached to the trailing edges of blades 1 and 7 also controlled the flow through the cascade to achieve periodicity. The blades were constructed by stereolithography with static pressure taps at the blade midspan incorporated into the stereolithography design.

Two types of endwalls were applied to the bottom wall of the blade cascade: a baseline flat endwall, and a three-dimensional non-axisymmetric contour. The top endwall remained flat for all studies. The design of the contour shape, depicted in Figure 2b, is described in further detail in Praisner et al. [15] and Knezevici et al. [16]. The contour generally consisted of a depression near the suction side and a peak near the pressure side in the forward portion of the passage, as well as a ridge running from the pressure side to the suction side through the aft portion of the passage. The highest point on the contour was approximately $0.06C_{ax}$ above the flat endwall height, while the lowest point on the contour was approximately $0.04C_{ax}$ below the flat endwall. The contouring was contained between the inlet and exit planes of the blade

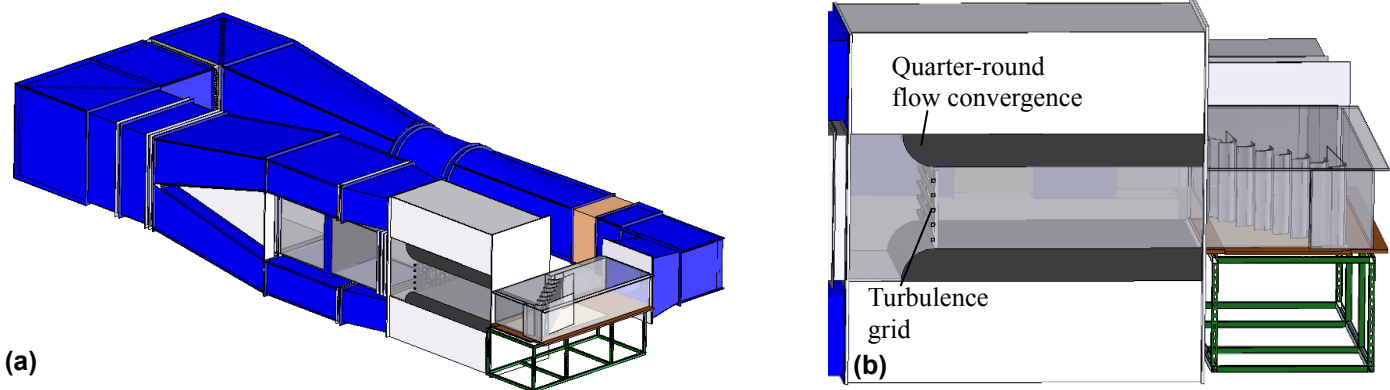


Figure 1. Depiction of the (a) large-scale low-speed wind tunnel, with a corner test section housing the Pack-B cascade, and (b) the inlet flow development section.

Table 1. Blade Geometry and Flow Conditions

Number of blades	7
Scale factor	8.6
Axial chord (C_{ax})	0.218 m
Pitch/chord (P/C_{ax})	0.826
Span/chord (S/C_{ax})	2.50
Inlet Re ($Re_{in} = C_{ax} U_{\infty,in} / \nu$)	1.25×10^5
Exit Re ($Re_{exit} = C_{ax} U_{\infty,exit} / \nu$)	2.00×10^5
Inlet velocity ($U_{\infty,in}$)	8.7 m/s
Inlet, exit flow angles	$35^\circ, 60^\circ$
Inlet, exit Mach	0.026, 0.042

cascade, and merged smoothly to the level of the flat endwall in the regions outside of the blade passage.

Endwall Heat Transfer Measurements

Heat transfer coefficients were measured on both the flat and contoured endwalls by imaging surface temperatures on uniform heat flux plates. The heat flux plates, depicted in Figure 2a, were manufactured in three sections, where the center section around the blades could be removed to install the flat or the contoured endwalls. For both endwall types, the heat flux plates consisted of serpentine inconel circuits encapsulated in kapton for a total thickness of $75 \mu\text{m}$, with a $37 \mu\text{m}$ copper layer adhered to the top surface to increase heat flux uniformity (Kang et al. [24]). The copper was painted with flat black paint to increase emissivity for infrared camera measurements. Type-E thermocouples were adhered to the bottom side of the kapton heater with thermal cement. A conduction bias of 0.8°C between the bottom and top heater surface temperature measurements was accounted for by a one-dimensional calculation of the heater thermal resistance.

For the flat endwall, the kapton heater was attached to a 3.2 mm thick lexan sheet ($k \approx 0.2 \text{ W/m}^2\text{-K}$), below which was a 12.7 mm thick closed-cell polyurethane foam ($k \approx 0.032 \text{ W/m}^2\text{-K}$) and a 12.7 mm thick medium density fiberboard support ($k \approx 0.12 \text{ W/m}^2\text{-K}$). The conductive thermal resistance of the contoured endwall assembly was matched to that of the flat endwall.

Due to the non-developable nature of the contoured endwall surface, the heat flux plate design was non-trivial. The kapton heater was adhered uniformly by a vacuum bag process to a 3.2 mm thick stereolithography surface ($k \approx 0.17 \text{ W/m}^2\text{-K}$) in the shape of the contour, as shown in Figure 2c. A mold was used to create a polyurethane foam body attached to the underside of the heat flux plate, where the top surface of the foam had the same shape as the contour and the bottom surface was flat.

The input heat flux of 1000 W/m^2 was calculated by measuring the input power to the inconel circuit and dividing by the heater area. The convective heat flux was then determined by subtracting conduction and radiation losses. Conduction losses through the bottom wall were estimated by a one-dimensional calculation, and subsequently verified by

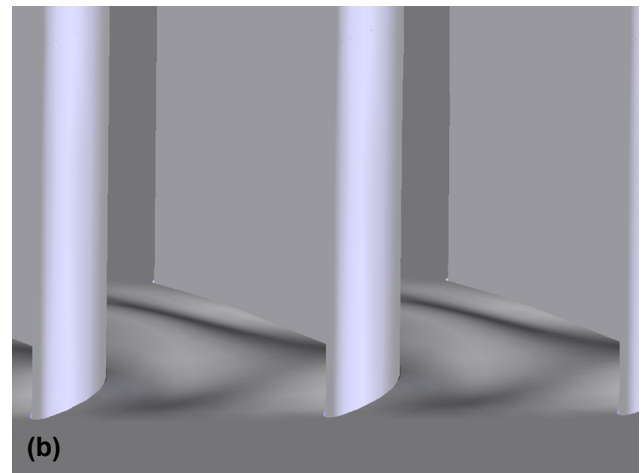
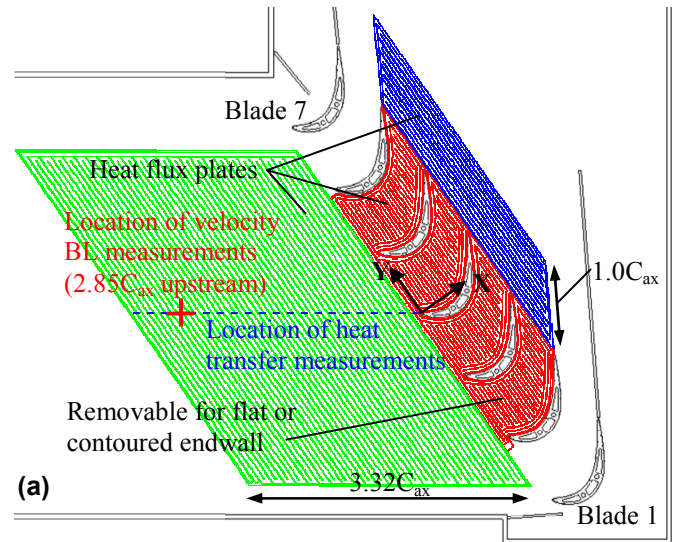


Figure 2. Schematic of the blade cascade with heat flux plates on the endwall (a); isometric view of the contoured endwall (b); and the contoured endwall heater mounted on a thin stereolithography plate (c).

thermocouple measurements, to be less than 2% of the input heat flux for both types of endwalls. Radiation losses from the high-emissivity endwalls were estimated to be less than 18% of

the input heat flux, assuming blackbody radiation exchange with isothermal surroundings at the freestream temperature. Both conduction and radiation loss corrections varied locally, with the highest corrections at the highest surface temperatures (nominally 44°C).

Surface temperatures on the bottom endwall were measured with an infrared camera by imaging the endwall from holes in the top endwall. These holes were covered during the test, and only opened to allow direct optical access when IR images were being acquired. Since the pressure differences between the inside and outside of the tunnel were very small, opening a hole in the top endwall did not affect the bottom endwall measurements, as determined by monitoring the endwall temperature before, during, and after image acquisition. The camera had a resolution of 1.4 pixels/mm, and a field of view of 320x240 pixels. Images were taken throughout the blade cascade to map the entire endwall, and assembled via an in-house computer code. At each image location, five images were taken and averaged, where each image was an average of 16 frames. Calibration of the images for emissivity and reflected temperature was performed by matching the image temperatures to the thermocouple readings. Typical values for emissivity and reflected temperature were $\epsilon=0.96$ and $T_{\text{reflc}}=10^\circ\text{C}$, which agreed well with the published value for flat black paint ($\epsilon=0.96$), as well as the average measured freestream temperature ($T_{\infty,\text{in}}=13^\circ\text{C}$). Calibrated infrared images generally agreed with the thermocouple measurements to within 0.3°C. No correction was performed for perspective distortion with the contoured endwall, since the moderate amount of three-dimensionality did not affect the camera focus.

Uncertainty in heat transfer measurements was estimated by the partial derivative method described by Moffat [25]. The largest source of uncertainty in the heat transfer was the measurement of surface temperature. The bias error was

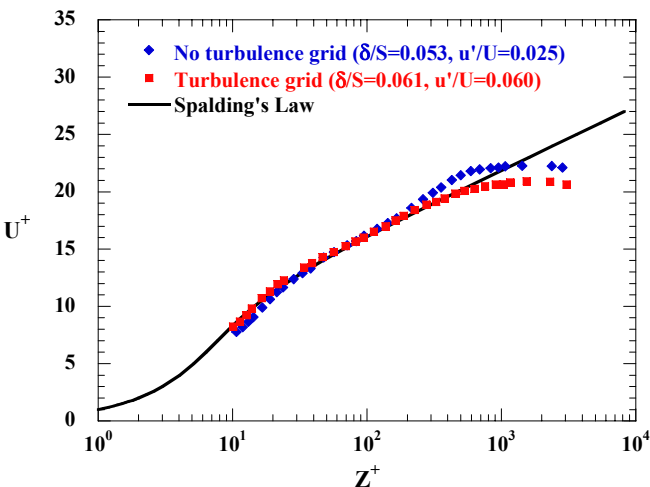


Figure 3. Inlet turbulent boundary layer measured $2.85C_{ax}$ upstream of blade 4 (see Figure 2a), with and without the turbulence grid installed.

estimated to be 0.7°C and was driven by infrared camera bias and thermocouple bias. The precision error of 0.3°C was determined by taking the standard deviation of six sets of infrared images, where each set contained five images. With a confidence interval of 95%, the total error in heat transfer was estimated to be $\partial\text{Nu}=4.0\%$ at a low value of $\text{Nu}=220$, and $\partial\text{Nu}=5.6\%$ at a high value of $\text{Nu}=358$.

Cascade Inlet Conditions

The velocity boundary layer upstream of the cascade and the turbulence level produced by the grid were measured to benchmark the inlet conditions. The streamwise component of velocity was measured with a single-component backscatter laser Doppler velocimeter, with velocity bias correction by residence time weighting. The red cross mark in Figure 2a indicates the location where the inlet boundary layer was measured, which was $2.85C_{ax}$ upstream of the center blade in the cascade. Boundary layer measurements were obtained with and without the turbulence grid installed, to ensure that the grid did not alter the flow unexpectedly. Figure 3 shows the streamwise component of velocity plotted in wall coordinates, which resembles a flat plate turbulent boundary layer. Note that the figure legend indicates the measured boundary layer thickness and freestream turbulence level. As expected, the addition of the turbulence grid results in a depressed wake region due to the higher freestream turbulence. Based on the measured boundary layer, a prediction of the boundary layer thickness at the blade inlet plane indicated that δ/S would be approximately 0.071. Refer to Table 2 for a summary of the measured inlet boundary layer parameters.

As shown in Figure 2a, the endwall heaters extended $3.32C_{ax}$ upstream of the blade cascade. This length was designed to minimize the unheated starting length effect on the measured endwall heat transfer. Figure 4 shows the development of the heat transfer coefficient along a line extending from the start of the heater to the leading edge of the center blade (see blue dashed line in Figure 2a). Underside-mounted thermocouples were used to determine the surface temperature near the start of the heater where optical access was not available, and IR thermography was used near the blade leading edge, along with the underside-mounted thermocouples. Both measurement methods agree well with each other where they overlap.

The measured Stanton numbers presented in Figure 4 were obtained with the turbulence grid installed. St values are

Table 2. Turbulent Boundary Layer Parameters at $2.85C_{ax}$ Upstream of Center Blade

Boundary layer thickness/span (δ/S)	0.061
Displacement thickness/span (δ^*/S)	0.0062
Momentum thickness/span (θ/S)	0.0046
Shape factor (H)	1.34
Momentum thickness Reynolds number (Re_θ)	1330
Freestream turbulence level (u'/U)	0.060

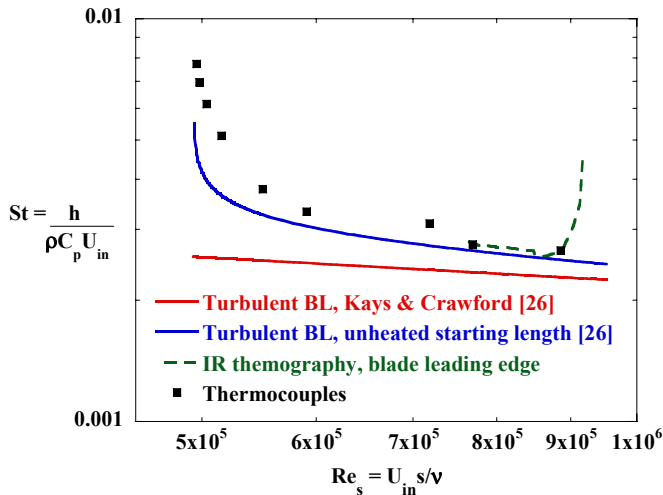


Figure 4. Heat transfer coefficient development along a line approaching blade 4 (see Figure 2a), with the turbulence grid installed.

slightly higher than the turbulent flat plate correlation of Kays and Crawford [26] with an unheated starting length. This is due to heat transfer augmentation by the high freestream turbulence, as noted by Thole and Bogard [27]. The increase in St for the IR thermography measurements at $Re_s > 9 \times 10^5$ is due to the effect of the horseshoe vortex augmenting endwall heat transfer in front of the blade leading edge.

To verify the turbulence grid design, the freestream turbulence level was measured along the centerline of the tunnel with a laser Doppler velocimeter, from 30 to 70 bar widths downstream of the grid ($7.10C_{ax}$ to $2.74C_{ax}$ upstream of the center blade). These measurements are shown in Figure 5, where the abscissa is the distance downstream of the grid normalized by the bar width. The measured turbulence decay followed the trend indicated by Baines and Peterson [18], and indicated a freestream turbulence level of 4% at the cascade inlet plane.

RESULTS AND DISCUSSION

The uniformity and periodicity of the flow around the blades was benchmarked by comparing the measured static pressure on the blade surfaces at midspan to a computational prediction. Figure 6 shows the midspan blade static pressure, normalized as a pressure coefficient, for blades 2-7 in the cascade. Excellent agreement with the prediction, and good periodicity across the cascade, is seen from examination of the flat endwall results. The midspan pressure distribution with a contoured endwall is also plotted for the center blade (blade 4) in Figure 6. The large blade aspect ratio and the relatively modest contouring result in a similar blade midspan static pressure distribution when compared to the flat endwall.

Oil Flow Visualization

Oil flow visualization with a mixture of oil and black paint was performed for both endwalls to provide a qualitative understanding of the effects of the three-dimensional

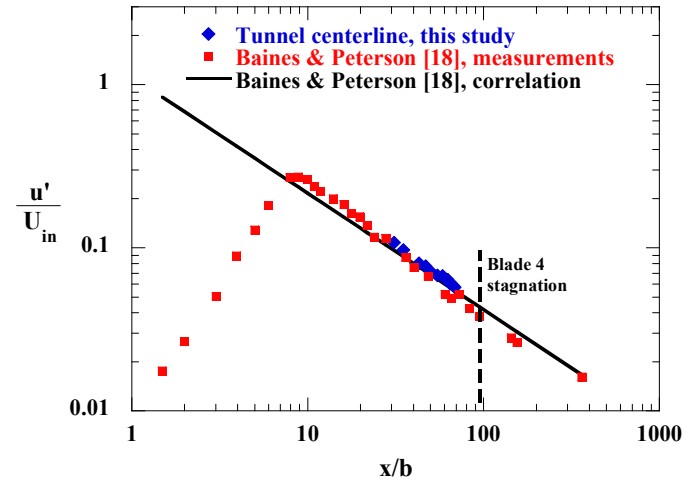


Figure 5. Freestream turbulence decay downstream of the turbulence grid, measured along the midspan centerline of the tunnel.

contouring on the endwall flow pattern. Visual interpretation of the paint streaks was used to draw streaklines to emphasize endwall flow patterns. In Figure 7a, the classic features of secondary flow are visible for the flat endwall. The saddle point region has an accumulation of paint and oil due to the separation of the inlet boundary layer as it rolls up into the horseshoe vortex in front of the leading edge of the blade. In the passage, a scoured region is seen where the passage vortex sweeps flow over the endwall from the pressure side to the suction side. Another scoured region attributed to a corner vortex is seen near the impingement location of the passage vortex on the blade suction side. The endwall streaklines near the pressure side-endwall corner tend to overturn toward the suction side, with respect to inviscid streamlines that would tend to follow the airfoil. This overturning is a result of the cross-passage pressure gradient acting on the new endwall boundary layer starting downstream of the inlet boundary layer separation.

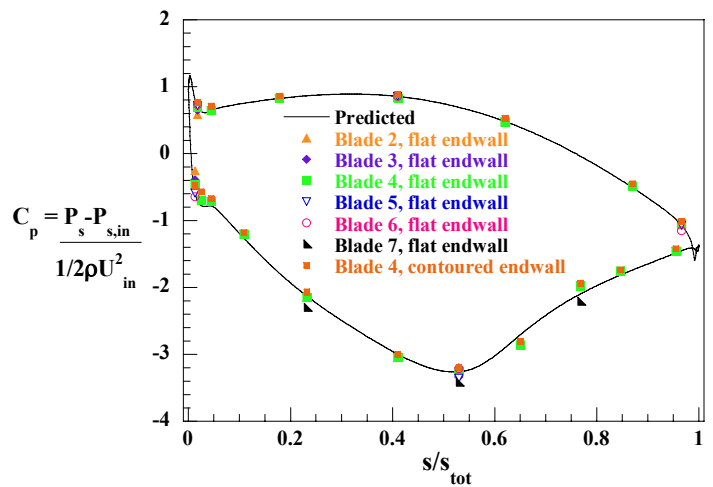


Figure 6. Blade static pressure distribution at the midspan plane for the flat and contoured endwalls.

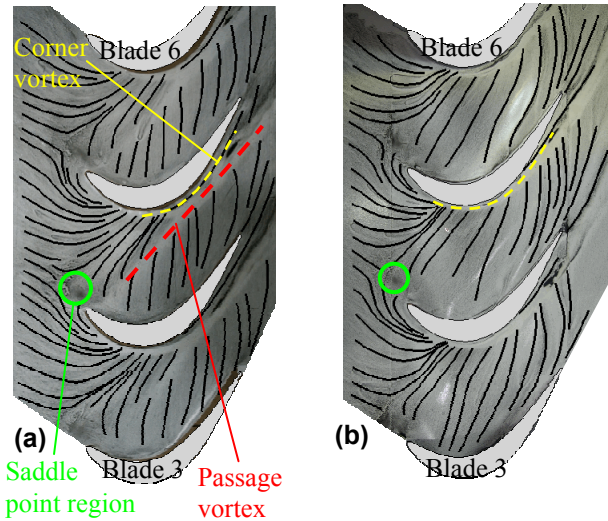


Figure 7. Qualitative interpretation of endwall streaklines from oil flow visualization on the (a) flat endwall and (b) contoured endwall.

The contoured endwall oil flow pattern in Figure 7b shows a remarkable difference in the passage when compared to the flat endwall (Figure 7a). The scoured region of the passage vortex is no longer apparent. Although it is less obvious, the saddle point region appears to have shifted slightly farther upstream, and the scoured region of the suction side corner vortex is closer to the leading edge of the blade, when compared to the flat endwall. In the passage, the overturning of the endwall streaklines near the pressure side appears to be reduced for the contoured endwall. However, further downstream the overturning is seen to increase, where the endwall contour merges back to the flat endwall level. This trend was also noted by Knezevici et al. [16], who attributed it to re-acceleration of the exit flow due to the lack of contouring downstream of the blade passage. Overall, the three-dimensional endwall contour has reduced the strength of the passage vortex and overturning of the near-wall flow in a large part of the passage, compared to a baseline flat endwall.

Endwall Heat Transfer

Flat endwall heat transfer results are presented in Figure 8 for the nominal cascade Reynolds number ($Re_{exit}=200,000$), where the heat transfer coefficients are non-dimensionalized as Nusselt numbers based on the blade axial chord. Good periodicity in the heat transfer measurements is seen by comparing the heat transfer patterns in each of the blade passages. The heat transfer contours in Figure 8 demonstrate the well-documented influence of secondary flows on endwall heat transfer. As the inlet boundary layer separates in front of the blade and is rolled up into the horseshoe vortex, the sweeping action of the vortex results in high heat transfer levels near the blade leading edge. The inlet boundary layer penetrates farther into the center of the passage, but is swept toward the suction side by the cross-passage pressure gradient.

High heat transfer is seen near the junction of the blade pressure side and the endwall, where a new boundary layer starts downstream of the separation of the inlet boundary layer. The effect of the passage vortex impinging on the blade suction side-endwall corner, and the presence of the corner vortex indicated by the flow visualization results (Figure 7a), both result in high Nusselt numbers near the trailing edge suction side of the blade. The effect of the blade wake is visible as a spike of high heat transfer that persists far downstream of the blade trailing edge.

Quantitative evaluations of endwall heat transfer results were obtained by extracting Nu values along streamwise and pitchwise lines in the cascade. For the streamwise line plots, inviscid streamline paths were obtained from a FLUENT [28] prediction of the blade midspan flowfield. Streamlines were released $0.46C_{ax}$ upstream of the cascade from three pitchwise locations, so that the streamlines would pass through $Y/P=0.25$, 0.50 and 0.75 at the inlet plane of the cascade. These streamlines are denoted as $0.25P$, $0.50P$, and $0.75P$, respectively. See the inset in Figure 9 for the paths of the streamlines superimposed on the flat endwall heat transfer contours. Extracted endwall results are presented as a function of the axial (X) coordinate of the streamline, normalized by the blade axial chord, so that $X/C_{ax}=0$ corresponds to the inlet plane of the cascade and $X/C_{ax}=1$ corresponds to the exit plane.

Nusselt numbers extracted from the contour plot of Figure 8 are plotted along the inviscid streamline paths in Figure 9. Data is extracted from two passages, where each passage is described by the blades surrounding it (i.e., passage 4-5 is between blades 4 and 5). Good periodicity is seen for the flat endwall results. Note that heat transfer coefficients are higher along the $0.25P$ streamline in Figure 9, as compared to the other streamlines through the passage. In general, Nu values increase through the passage and then begin to decay downstream of the trailing edge plane ($X/C_{ax}>1$).

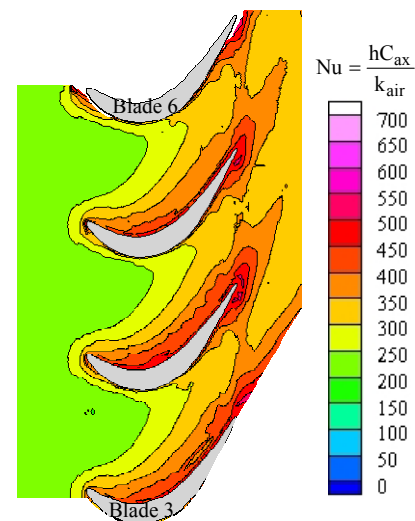


Figure 8. Contours of endwall Nusselt number for the flat endwall.

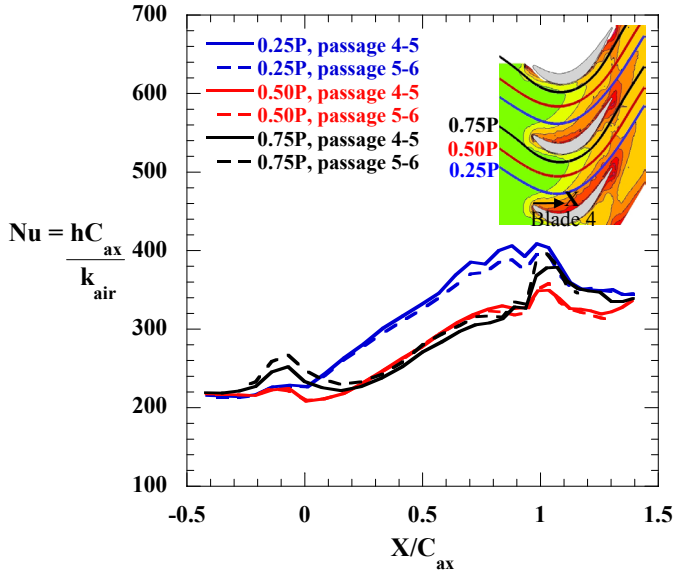


Figure 9. Nusselt numbers for the flat endwall, plotted along inviscid streamlines passing through 0.25P, 0.50P, and 0.75P (see inset).

The data presented in Figure 10 was extracted from Figure 8 along pitchwise lines, as shown in the inset in Figure 10. Note that the pitchwise coordinate (Y) is normalized by the blade pitch and is referenced from the camber line of the blade (i.e., $Y/P=0$ starts at the camber line and $Y/P=1$ ends at the camber line of the adjacent blade above). When comparing the different axial locations plotted in Figure 10, it was noted that the highest pitchwise gradients in Nu are near the forward part of the passage ($0.25C_{ax}$), as compared to the other pitchwise locations. Note from Figure 2 that the endwall contouring is also strongest around this location.

Contoured endwall heat transfer was compared to the flat endwall heat transfer through an augmentation parameter. Figure 11 was generated by taking the local differences in heat transfer coefficients between the contoured and flat endwalls, and then normalizing by the flat endwall heat transfer. Values less than 0 indicate that the contoured endwall produces lower heat transfer levels than the flat endwall. Figure 11 shows a negative augmentation along most of the pressure surface of the blade. This is especially significant since it occurs in a region of nominally high heat transfer coefficients. The reduced crossflow seen in Figure 7b as compared to Figure 7a would likely result in lower heat transfer levels for the new boundary layer downstream of the horseshoe vortex separation. Negative augmentation also occurs along the downstream portion of the suction side of the blade. A weakening of the horseshoe and passage vortices due to non-axisymmetric endwall contouring reduces the strength of the corner vortex and thus the associated heat transfer. Sieverding [29] indicates that the corner vortex develops from the impingement of the pressure side leg of the horseshoe vortex on the blade suction side.

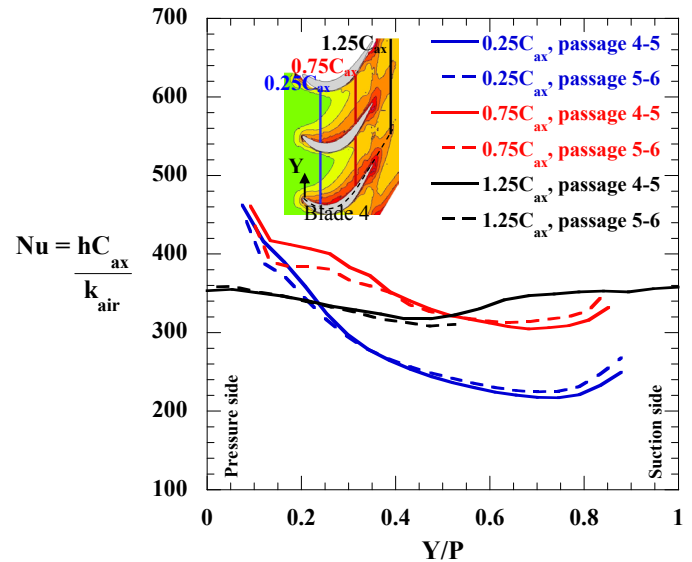


Figure 10. Nusselt numbers for the flat endwall, plotted along pitchwise lines at $0.25C_{ax}$, $0.75C_{ax}$, and $1.25C_{ax}$ from the leading edge (see inset).

In Figure 11, positive augmentations are seen near the leading edge in the corner between the endwall and blade suction side, possibly indicating a stronger suction side horseshoe vortex as found by Gustafson [14]. Near the saddle point region, augmentation levels are also high. However, the magnitudes of Nu in Figure 8 are relatively low at this location, thereby indicating that the contoured endwall is not severely impacting the endwall. Slightly downstream of the exit plane of the passage, augmentation levels tend to increase, which could be attributed to the stronger crossflow that develops there for the contoured endwall relative to the flat endwall.

Data extracted from the augmentation contour is plotted along the inviscid streamline paths in Figure 12. Note that the highest level of augmentation occurs along the 0.25P streamline where it passes through the saddle point region. The

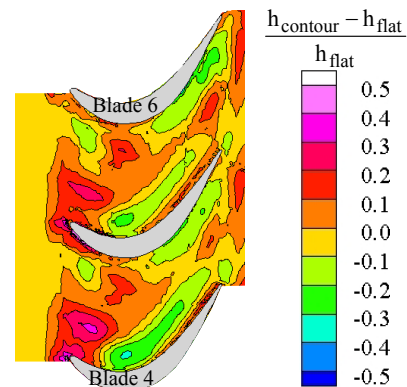


Figure 11. Contours of heat transfer coefficient augmentation for the flat versus contoured endwalls.

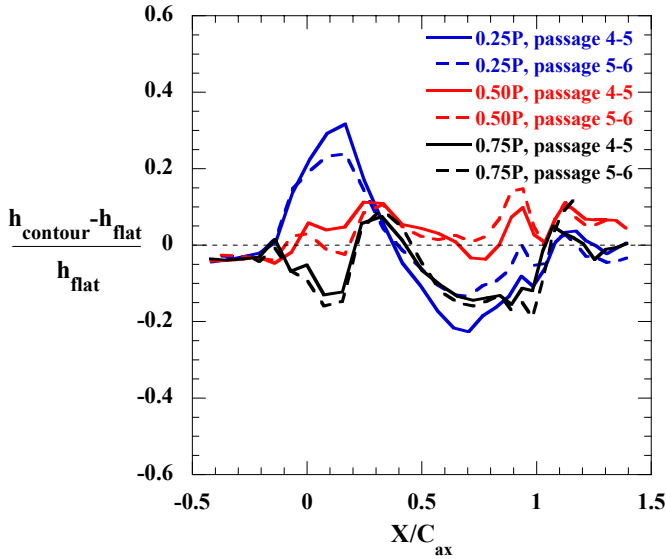


Figure 12. Heat transfer coefficient augmentation along inviscid streamline paths (see Figure 9).

lowest level of augmentation occurs near the pressure side of the passage (0.25P streamline), with low augmentation also present along the suction side of the passage (0.75P streamline) toward the trailing edge.

Heat transfer augmentation is plotted along the pitchwise lines through the passage in Figure 13. At $0.25C_{ax}$, the contoured endwall shows decreased heat transfer (negative augmentation) relative to the flat endwall near the pressure side from $Y/P=0.1$ to $Y/P=0.25$, but increased heat transfer in the saddle point region around $Y/P=0.35$. Recall, however, that the magnitude of Nu is low around $Y/P=0.35$ (refer to Figure 10), so that high augmentation is not as meaningful. Further into the passage ($0.75C_{ax}$ in Figure 13), the contoured endwall has overall lower heat transfer than the flat endwall. Downstream of the cascade at $1.25C_{ax}$, augmentation values indicate nearly the same heat transfer coefficients for the flat and contoured endwalls, which would be expected since the contouring does not continue past the trailing edge plane ($X/C_{ax}=1.0$).

When averaging over all passages, from the leading edge plane ($X/C_{ax}=0$) to the trailing edge plane ($X/C_{ax}=1.0$), the contoured endwall results in a 3.1% reduction in area-averaged heat transfer. Peaks and valleys in the contoured endwall shape cause it to have a slightly larger surface area than the flat endwall (1.3% larger). The combination of the heat transfer reduction and the larger surface area indicate that the contoured endwall will have a slightly lower overall heat load (average heat transfer coefficient multiplied by surface area) than a flat endwall:

$$\frac{\overline{h_{contour}}}{\overline{h_{flat}}} \frac{A_{contour}}{A_{flat}} = 0.969 * 1.013 = 0.98 \quad (1)$$

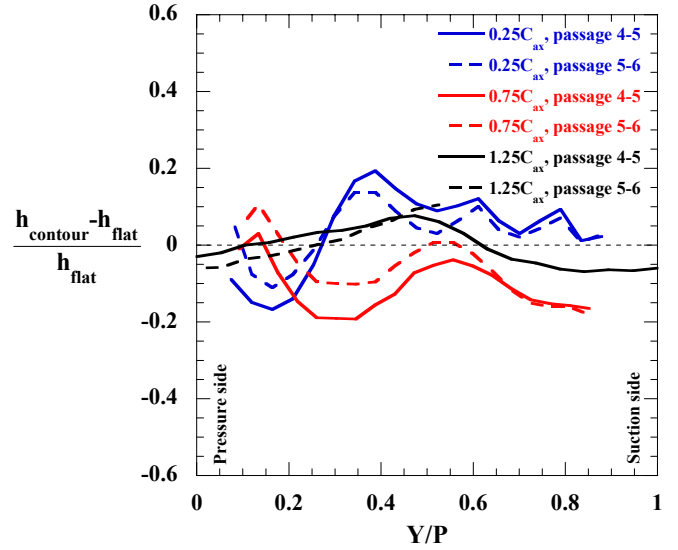


Figure 13. Heat transfer coefficient augmentation along pitchwise lines (see Figure 10).

More importantly, the reduced local heat load in high heat transfer regions for the contoured endwall (refer to Figure 11) may improve the overall turbine part durability.

Cascade Reynolds Number Effect

To test the robustness of the contoured endwall to off-design conditions, heat transfer coefficients were obtained for the flat and contoured endwalls at cascade Reynolds numbers lower and higher than the nominal condition of $Re_{exit}=200,000$. Figure 14 shows contour plots of flat endwall Nusselt numbers for three Reynolds numbers. As expected, Nu increases with increasing Re_{exit} for the flat endwall. At a location approximately $0.5C_{ax}$ upstream of the cascade, the measured change in Nu as the Reynolds number increased from $Re_{exit}=118,000$ to $307,000$ was within 7% of the expected change based on flat plate turbulent boundary layer correlations. For the range of Re_{exit} tested, the endwall heat transfer features described earlier for the flat endwall do not appear to be significantly different between the various cascade Reynolds number cases.

The heat transfer augmentation of the contoured versus flat endwalls for various cascade Reynolds numbers is shown in Figure 15. Note that for most of the passage the augmentation does not appear to change for the range of Reynolds numbers tested, which suggests that the effect of the contour on endwall heat transfer would not be strongly dependent on the turbine operating condition. Figure 16 shows the augmentation extracted along the streamwise paths. Again, the augmentation of the contoured endwall appears to be fairly consistent for a range of cascade Reynolds numbers.

CONCLUSIONS

A low-pressure turbine blade cascade based on the Pack-B airfoil geometry was developed for the purpose of testing the

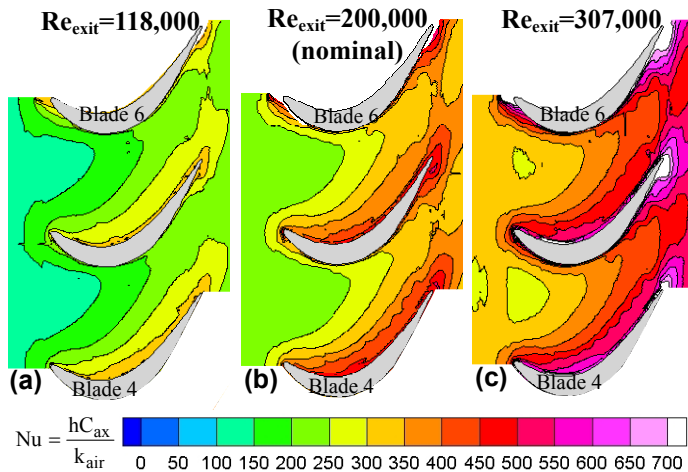


Figure 14. Contours of Nusselt number for the flat endwall at (a) $Re_{exit}=118,000$, (b) $Re_{exit}=200,000$ (nominal), and (c) $Re_{exit}=307,000$.

effects of three-dimensional endwall contouring on endwall heat transfer. Heat transfer measurements were obtained for a baseline flat endwall, as well as for a contoured endwall geometry, for three cascade exit Reynolds numbers. Oil flow visualization was used to determine the effects of the contouring on the near-wall flow.

The oil flow visualization for the flat endwall showed the classic features of secondary flow, including a scoured region describing the path of the passage vortex from pressure to suction side, and overturning of endwall streamlines near the blade pressure side-endwall corner. When the contour was present, the scoured region was not visible, indicating reduced passage vortex strength. Also, the overturning of endwall streamlines near the pressure side was reduced, as compared to the flat endwall, suggesting a reduced effect of the cross-passage pressure gradient on the endwall boundary layer.

The features of the flat endwall heat transfer measurements agreed with the well-documented effects of the leading edge

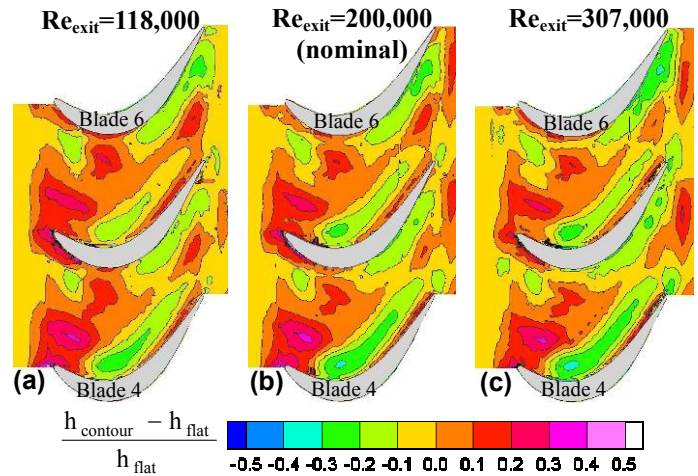


Figure 15. Contours of heat transfer augmentation for (a) $Re_{exit}=118,000$, (b) $Re_{exit}=200,000$ (nominal), and (c) $Re_{exit}=307,000$.

horseshoe vortex, the cross-passage flow, the new endwall boundary layer downstream of the separation line, and the blade wake on endwall heat transfer.

The contoured endwall heat transfer results were compared to the flat endwall through an augmentation parameter. Augmentation levels were high near the saddle point, but were as low as -20% near the blade pressure side-endwall corner. Low augmentation levels were also seen near the suction side of the blade, around the region where the passage vortex impinges on the blade. This reduction was likely due to the decreased effect of the passage vortex on the endwall with contouring, as seen in the oil flow visualization results. Area-averaged heat transfer was reduced by 3.1% for the contoured endwall versus a flat endwall.

The effect of contouring on the endwall heat transfer was tested for off-design performance by measuring heat transfer coefficients at cascade exit Reynolds numbers lower and higher than the nominal value. No major change in the endwall heat

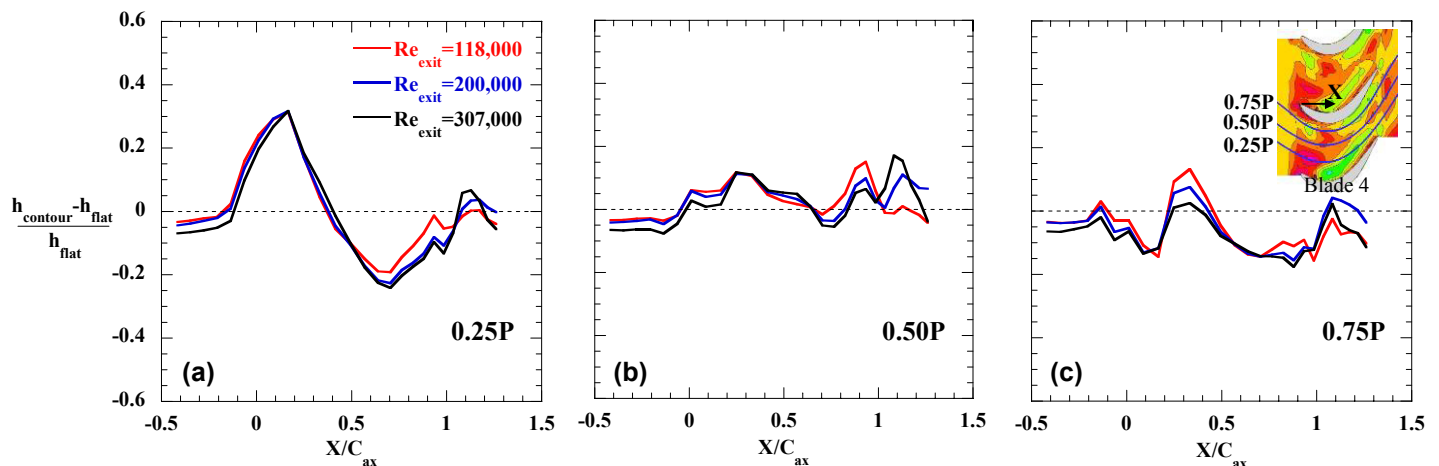


Figure 16. Contoured versus flat endwall heat transfer augmentation at various cascade exit Reynolds numbers, plotted along the inviscid streamlines passing through (a) 0.25P, (b) 0.50P, and (c) 0.75P (see inset).

transfer pattern was noted for the flat endwall over the range of Reynolds numbers tested. Also, the effect of the contour on endwall heat transfer was not dependent on cascade exit Reynolds number.

ACKNOWLEDGMENTS

The authors gratefully acknowledge United Technologies—Pratt & Whitney for their support of this work, and Eunice Allen-Bradley for performing the endwall contour design. The authors would also like to thank Steven Walker for his help with test section construction.

REFERENCES

- [1] Langston, L.S., 1980, "Crossflows in a Turbine Passage," *Journal of Engineering for Power*, Vol. 102, pp. 866-874.
- [2] Sharma, O.P. and Butler, T.L., 1987, "Predictions of Endwall Losses and Secondary Flows in Axial Flow Turbine Cascades," *Journal of Turbomachinery*, Vol. 109, pp. 229-236.
- [3] Goldstein, R.J. and Spores, R.A., 1988, "Turbulent Transport on the Endwall in the Region Between Adjacent Turbine Blades," *Journal of Heat Transfer*, Vol. 110, pp. 862-869.
- [4] Boletis, E., 1985, "Effects of Tip Endwall Contouring on the Three-Dimensional Flow field in an Annular Turbine Nozzle Guide Vane: Part I—Experimental Investigation," *Journal of Engineering for Gas Turbines and Power*, Vol. 107, pp. 983-990.
- [5] Morris, A.W.H. and Hoare, R.G., 1975, "Secondary Loss Measurements in a Cascade of Turbine Blades with Meridional Wall Profiling," ASME Paper No. 75-WA/GT-13.
- [6] Lin, Y.-L. and Shih, T. I.-P., 2000, "Flow and Heat Transfer in a Turbine Nozzle Guide Vane with Endwall Contouring," AIAA Paper No. AIAA-2000-3002.
- [7] Harvey, N.W., Rose, M.G., Taylor, M.D., Shahpar, S., Hartland, J., and Gregory-Smith, D., 2000, "Non-Axisymmetric Turbine End Wall Design: Part I—Three-Dimensional Linear Design System," *Journal of Turbomachinery*, Vol. 122, pp. 278-285.
- [8] Hartland, J., Gregory-Smith, D., Harvey, N.W., and Rose, M.G., 2000, "Non-Axisymmetric Turbine End Wall Design: Part II—Experimental Validation," *Journal of Turbomachinery*, Vol. 122, pp. 286-293.
- [9] Brennan, G., Harvey, N.W., Rose, M.G., Fomison, N., and Taylor, M.D., 2003, "Improving the Efficiency of the Trent 500-HP Turbine Using Non-axisymmetric End Walls: Part I—Turbine Design," *Journal of Turbomachinery*, Vol. 125, pp. 497-504.
- [10] Rose, M.G., Harvey, N.W., Seaman, P., Newman, D.A., and McManus, D., 2001, "Improving the Efficiency of the Trent 500-HP Turbine Using Non-axisymmetric End Walls. Part II: Experimental Validation," ASME Paper No. 2001-GT-0505.
- [11] Germain, T., Nagel, M., Raab, I., Scheupbach, P., Abhari, R.S., and Rose, M., 2008, "Improving Efficiency of a High-Work Turbine Using Non-Axisymmetric Endwalls Part I: Endwall Design and Performance," ASME Paper No. GT2008-50469.
- [12] Scheupbach, P., Abhari, R.S., Rose, M., Germain, T., Raab, I., and Gier, J., 2008, "Improving Efficiency of a High-Work Turbine Using Non-Axisymmetric Endwalls Part II: Time-Resolved Flow Physics," ASME Paper No. GT2008-50470.
- [13] Saha, A.K. and Acharya, S., 2008, "Computations of Turbulent Flow and Heat Transfer Through a Three-Dimensional Nonaxisymmetric Blade Passage," *Journal of Turbomachinery*, Vol. 130, pp. 031008-1-10.
- [14] Gustafson, R., Mahmood, G., and Acharya, S., 2007, "Aerodynamic Measurements in a Linear Turbine Blade Passage with Three-Dimensional Endwall Contouring," ASME Paper No. GT2007-28073.
- [15] Praisner, T.J., Allen-Bradley, E., Grover, E.A., Knezevici, D.Z., and Sjolander, S.A., 2007, "Application of Non-Axisymmetric Endwall Contouring to Conventional and High-Lift Airfoils," ASME Paper No. GT2007-27579.
- [16] Knezevici, D.Z., Sjolander, S.A., Praisner, T.J., Allen-Bradley, E., and Grover, E.A., 2008, "Measurements of Secondary Losses in a Turbine Cascade with the Implementation of Non-axisymmetric Endwall Contouring," ASME Paper No. GT2008-51311.
- [17] Praisner, T.J., Grover, E.A., Knezevici, D.C., Popovic, I., Sjolander, S.A., Clark, J.P., and Sondergaard, R., 2008, "Toward the Expansion of Low-Pressure-Turbine Airfoil Design Space," ASME Paper No. GT2008-50898.
- [18] Baines, W.D. and Peterson, E.G., 1951, "An Investigation of Flow Through Screens," *Transactions of the ASME*, 1951.
- [19] Lake, J. P., King, P. I., and Rivir, R. B., 1999, "Reduction of Separation Losses on a Turbine Blade with Low Reynolds Numbers", AIAA Paper No. 99-0242.
- [20] Murawski, C. G., and Vafai, K., 2000, "An Experimental Investigation of the Effect of Freestream Turbulence on the Wake of a Separated Low Pressure Turbine Blade at Low Reynolds Numbers", *Journal of Fluids Engineering*, Vol. 122, pp. 431-433.
- [21] Mahallati, A., McAuliffe, B.R., Sjolander, S.A., and Praisner, T., 2007, "Aerodynamics of a Low-Pressure Turbine Airfoil at Low Reynolds Numbers Part I: Steady Flow Measurements", ASME Paper No. GT2007-27347.
- [22] Zoric, T., Popovic, I., Sjolander, S.A., Praisner, T., and Grover, E., 2007, "Comparative Investigation of Three Highly-Loaded LP Turbine Airfoils: Part I – Measured Profile and Secondary Losses at Design Incidence", ASME Paper No. GT2007-27537.
- [23] Popovic, I., Zhu, J., Dai, W., Sjolander, S.A., Praisner, T.J. and Grover, E.A., 2006, "Aerodynamics of a Family of Three Highly Loaded Low-Pressure Turbine Airfoils: Measured Effects of Reynolds Number and Turbulence

- Intensity in Steady Flow,” ASME Paper No. GT2006-91271.
- [24] Kang, M. B., Kohli, A., and Thole, K. A., 1999, “Heat Transfer and Flowfield Measurements in the Leading Edge Region of a Stator Vane Endwall,” *Journal of Turbomachinery*, Vol. 121, pp. 558-568.
- [25] Moffat, R. J., 1988, “Describing the Uncertainties in Experimental Results,” *Experimental Thermal and Fluid Science*, Vol. 1, pp. 3-17.
- [26] Kays, W. M. and Crawford, M. E., 1980, *Convective Heat and Mass Transfer* (2nd ed.), McGraw-Hill, New York, pp. 216-217.
- [27] Thole, K. A. and Bogard, D. G., 1995, “Enhanced Heat Transfer and Shear Stress Due to High Freestream Turbulence,” *Journal of Turbomachinery*, Vol. 117, pp. 418-424.
- [28] FLUENT (version 6.3.26), Fluent Inc., Lebanon, NH.
- [29] Sieverding, C.H., 1985, “Recent Progress in the Understanding of Basic Aspects of Secondary Flows in Turbine Blade Passages,” *Journal of Engineering for Gas Turbines and Power*, Vol. 107, pp. 248-257.